

Direct Distance Measurements to Superluminal Radio Sources

D. C. Homan¹ and J. F. C. Wardle²
Physics Department, Brandeis University
Waltham, MA 02454

Accepted for publication in The Astrophysical Journal

ABSTRACT

We present a new technique for directly measuring the distances to superluminal radio sources. By comparing the observed proper motions of components in a parsec scale radio jet to their measured Doppler factors, we can deduce the distance to the radio source independent of the standard rungs in the cosmological distance ladder. This technique requires that the jet angle to the line of sight and the ratio of pattern to flow velocities are sufficiently constrained. We evaluate a number of possibilities for constraining these parameters and demonstrate the technique on a well defined component in the parsec scale jet of the quasar 3C 279 ($z = 0.536$). We find an angular size distance to 3C 279 of greater than $1.8_{-0.3}^{+0.5}\eta^{1/8}$ Gpc, where η is the ratio of the energy density in the magnetic field to the energy density in the radiating particles in that jet component. For an Einstein-de Sitter Universe, this measurement would constrain the Hubble constant to be $H_0 \lesssim 65\eta^{-1/8}$ km/s/Mpc at the two sigma level. Similar measurements on higher redshift sources may help discriminate between cosmological models.

Subject headings: distance scale – galaxies: active – galaxies: distances and redshifts – galaxies: kinematics and dynamics – quasars: individual (3C 279) – radiation mechanisms: non-thermal

1. Introduction

To answer fundamental questions about the geometry of the Universe and the distribution of matter on the largest scales we must be able to measure the distance to objects at large redshift. Type Ia supernovae have begun to fill this role and recent results suggest that the overall expansion of the Universe may be accelerating (Riess et al. 1998; Perlmutter et al. 1999). The great brightness of Type Ia supernovae, which can out-shine their parent galaxies, allow them to be observed up to redshifts of $z = 1$. It is important to have cosmological probes at even higher redshifts where we are less sensitive to local perturbations (Tipler 1999) and the predictions of different cosmological models become more distinct (Carroll, Press & Turner 1992).

Quasars are regularly observed at very large redshifts and provide an alternative to gravitational lenses for high redshift cosmology studies. Optically, it is difficult to define a standard candle for quasars because of the wide range of intrinsic luminosities between objects and the high degree of variability of individual objects. Similar difficulties exist with using the radio luminosity for the $\sim 10\%$ of objects that are radio loud. Global Very Long Baseline Interferometry (VLBI) arrays offer an alternative to defining a standard candle. The ability to resolve compact structures and observe proper motions in the radio jets of many sources suggests the possibility of defining a standard rod from which angular size distances may be derived.

Kellermann (1993) defined a standard rod for compact radio sources as the distance between the core and the most distant jet component whose peak brightness exceeds 2% of the core brightness. He used data from 82 compact sources (out to

¹dch@quasar.astro.brandeis.edu

²jfcw@quasar.astro.brandeis.edu

$z \approx 3$) and found an observed relation between angular size and redshift which is consistent with an Einstein-de Sitter Universe (deceleration parameter, $q_0 = 0.5$).

Lynden-Bell (1977) and Lynden-Bell and Liller (1978) combined early proper motion measurements with a light-echo model, e.g. (Couderc 1939), in the first attempts to use proper motions observed in radio jets as cosmological distance indicators. Several authors have examined the statistics of proper motions of patterns in radio jets as a cosmological probe. Yahil (1979) proposed the idea of a proper motion-redshift diagram to measure Hubble's constant and the deceleration parameter. Cohen et al. (1988) used measured proper motion data and a simple beaming model to show that the upper envelope of the proper motion data decreased with redshift in a manner consistent with a Friedmann cosmology and inconsistent with several alternatives. More recently, Vermeulen and Cohen (1994) have refined these ideas and used a much larger sample to explore the possibility of measuring cosmological parameters with proper motion data. They found they could usefully constrain cosmological parameters and simultaneously learn about the distribution of jet parameters.

Our approach differs from these techniques in that we use VLBI observations to directly measure the distance to *individual* superluminal radio sources. We compare the proper motions of individual components in a parsec-scale radio jet with measurements of their Doppler factors. In addition, we must constrain the angle the component motion makes with the line of sight and separate the pattern speed (observed in proper motion measurements) from the flow speed (observed in Doppler factor measurements). In §2 we present a number of possibilities for constraining these parameters, and in §3 we evaluate the technique with an example, using a well defined component in the VLBI jet of the quasar 3C 279. Section 4 discusses the measurement errors and systematic uncertainties associated with this technique. Section 5 explores the application of such measurements to cosmological questions. Our conclusions are presented in §6.

2. Theory

The observed proper motion, μ , of a pattern (component) in a parsec-scale radio jet depends on the intrinsic pattern speed, β_p , the angle between the jet axis and the line to the observer, θ , and the angular size distance to the radio source, D_A .

$$\mu = \frac{c}{D_A(1+z)} \frac{\beta_p \sin \theta}{1 - \beta_p \cos \theta} = \frac{c}{D_A(1+z)} \beta_a \quad (1)$$

where β_a is the apparent transverse velocity of the component in units of the speed of light.

We define a Doppler factor for the pattern, δ_p , by

$$\delta_p = \frac{\sqrt{1 - \beta_p^2}}{1 - \beta_p \cos \theta}. \quad (2)$$

The aberrated angle, θ' , is the angle between the jet axis and the line to the observer in the frame that moves along the jet with the pattern speed. It is given by

$$\cos \theta' = \frac{\cos \theta - \beta_p}{1 - \beta_p \cos \theta} = \cos \theta - \beta_a \sin \theta \quad (3)$$

and

$$\sin \theta' = \delta_p \sin \theta. \quad (4)$$

We can use these relations to derive an expression for the angular size distance:

$$D_A = \frac{c}{\mu(1+z)} \left(\frac{\sqrt{\delta_p^2 + \cos^2 \theta' - 1 - \delta_p \cos \theta'}}{\sqrt{1 - \cos^2 \theta'}} \right). \quad (5)$$

Equation 5 is plotted for various values of δ_p in figure 1. In this equation μ is in natural units of rad/sec; however, in figure 1 μ is in units of mas/year.

The proper motion μ is a directly observed quantity. The Doppler factor of the pattern, δ_p , is indirectly observed through the use of Synchrotron Self-Compton (SSC) or equipartition arguments (see §2.2 and the appendix) which measure a product of Doppler factors:

$$\delta_{SSC} = \delta_p (\delta'_f)^{\frac{2\alpha+3}{2\alpha+4}} \quad (6)$$

and

$$\delta_{eq} = \delta_p (\delta'_f)^{\frac{2\alpha+5}{2\alpha+6}} \quad (7)$$

where α is the spectral index ($S \propto \nu^{-\alpha}$) for optically thin synchrotron radiation and δ'_f is the Doppler factor of the fluid frame relative to the pattern frame:

$$\delta'_f = \frac{\sqrt{1 - (\beta'_f)^2}}{1 - \beta'_f \cos \theta'} \quad (8)$$

where θ' is the angle of observation in the pattern frame and β'_f is the speed of the fluid in the pattern frame.

For comparison to proper motion measurements, we are interested in δ_p . To determine δ_p from equipartition or SSC arguments we must measure or usefully constrain δ'_f which typically requires measuring the pattern versus flow speed; however, there is a useful constraint we can place on δ'_f if we know θ' . For a given θ' , the maximum in δ'_f is when $\beta'_f = \cos \theta'$, so

$$\delta'_f \leq 1/\sqrt{1 - (\cos \theta')^2}. \quad (9)$$

2.1. Additional Constraints

In the sections that follow, we explore a number of constraints that allow us to turn measurements of proper motions and Doppler factors into direct distance measurements. Some of these techniques allow measurement or constraint of δ'_f which is important for accurate determination of δ_p from Doppler factor measurements.

2.1.1. Bent Jets

For a given pattern speed, β_p , the observed proper motion is maximized when $\cos \theta = \beta_p$. At this critical angle, $\cos \theta' = 0$ and equation 5 reduces to:

$$D_A = \frac{c\sqrt{\delta_p^2 - 1}}{\mu(1+z)} \quad (10)$$

Sources inside the critical angle will give an upper limit on D_A , and sources outside the critical angle will give a lower limit. However, these limits will only be useful for sources near the critical angle, and for these sources, we need an additional

constraint to determine their orientation relative to the critical angle.

Jets which bend on VLBI scales give a unique opportunity for observing a source at or near its critical angle. As a component on a curved trajectory passes through the critical angle, a number of observable effects occur: the proper motion of the component maximizes, the orthogonal component of the magnetic field (projected in the plane of the sky) maximizes creating a maximum or minimum in the observed linear polarization, and thin features, such as shocks, minimize in observed aspect ratio.

We note that if the flow and pattern have different speeds they will also have different critical angles. The maximization of the proper motion occurs at the pattern's critical angle. Any maximum or minimum in the observed linear polarization depends on the flow's critical angle. Observing both critical angles provides a method of resolving the difference between the flow and pattern speeds. If only the critical angle of the pattern is observed, a useful constraint is that the Doppler factor for the flow as observed from the pattern frame, δ'_f , has a maximum value of 1 (see equation 9).

2.1.2. Aspect Ratio

Several authors have made use of a sharp (narrow) feature in a radio jet to measure or constrain the jet angle to the line of sight (Eichler & Smith 1983; Biretta, Owen & Hardee 1983; Biretta, Owen & Cornwell 1989; Unwin & Wehrle 1992). A sharp feature, assumed to be oriented perpendicular to the jet direction, is a sign that the pattern is moving at close to its critical angle. The shape an observer sees for a component moving in a radio jet is governed by the aberration between the pattern frame and observer frame.

The observed aspect ratio of a component is the ratio of its extent along the jet to its extent transverse to the jet, $\zeta = size_{\parallel}/size_{\perp}$ (see figure 2). The ratio ζ constrains $\cos \theta'$ if the pattern is assumed to be axially symmetric and oriented perpendicular to the direction of motion. Under these circumstances, $\zeta \geq |\cos \theta'|$ and we obtain potentially useful limits on the angular size distance (from equation 5, corresponding to positive

and negative signs for $\cos \theta'$:

$$D_A \geq \frac{c}{\mu(1+z)} \left(\frac{\sqrt{\delta_p^2 + \zeta^2 - 1 - \delta_p \zeta}}{\sqrt{1 - \zeta^2}} \right) \quad (11)$$

and

$$D_A \leq \frac{c}{\mu(1+z)} \left(\frac{\sqrt{\delta_p^2 + \zeta^2 - 1 + \delta_p \zeta}}{\sqrt{1 - \zeta^2}} \right) \quad (12)$$

Because the SSC technique produces only a lower limit on the Doppler factor (Marscher 1987), only the lower limit on D_A will be applicable when we determine δ_p using that technique. The equipartition assumption will also produce a lower limit on the Doppler factor if we only have an upper limit on the frequency of the self-absorption turnover in the synchrotron spectrum (Readhead 1994).

It is important to note that the relations developed here assume that the pattern is perpendicular to the jet direction and not oblique. Obliqueness in the plane of the sky is observable from the orientation of the feature and perhaps its linear polarization. Assuming it is not very large, this kind of obliqueness can be corrected for; however, if a component can be oblique in the plane of the sky it may also be oblique in the plane of observation. Obliqueness in the plane of observation is indistinguishable from effects of aberration for determining the observed component dimensions and may cause the relation $\zeta \geq |\cos \theta'|$ to be violated. Uncertainty in the degree of obliqueness of a given component is equivalent to an added uncertainty in the measurement of ζ (Biretta, Owen & Cornwell 1989; Unwin & Wehrle 1992).

2.1.3. Linear Polarization

The linear polarization of a pattern in a radio jet provides a measure of the magnetic field order. For a tangled magnetic field which has been compressed (due perhaps to a propagating shock), the degree of linear polarization observed depends both upon the degree of compression and the viewing angle (Laing 1980; Hughes, Aller & Aller 1985). The highest degrees of parallel linear polarization (for a given compression) will be observed when the flow is moving at or near its critical angle. The degree of compression can be

related to the speeds of the flow (upstream and downstream) relative to the propagating shock, e.g. (Cawthorne & Wardle 1988; Hughes, Aller & Aller 1989).

Wardle et al. (1994) work out a complete model for deducing the jet angle to the line of sight and pattern versus flow speeds from detailed VLBI polarization data. They consider the general case of a compression in a jet with a tangled field plus a component of ordered field along the axis of compression. By measuring the degree of linear polarization and total intensity in both the shocked and un-shocked regions in the jet of 3C 345 ($z = 0.595$), they were able to constrain the flow speed relative to the shock and the inclination of the jet to the line of sight.

To illustrate the use of the constraints available from linear polarization observations, we will start with the results of Wardle et al. (1994) for jet component C3 of 3C 345. The reader is referred to that paper for details. For their 1984.2 epoch, they find nominal values of $\theta = 2.5^\circ/D_A$, $\beta_d = 0.5$, and $\beta_a = 11.1D_A$ ($\mu = 0.44$ mas/year). The flow speed of the shocked fluid towards the core in the frame of the shock-front is β_d . In the notation of this paper, $\beta'_f = -\beta_d$. D_A is measured in Gpc for the values given above.

We use equations 3 and 7 to calculate $\cos \theta' = 0.5$ and $\delta'_f = 0.7$ which are essentially independent of distance. If we had observations of the synchrotron self-absorption turnover for component C3 in 3C 345 at this epoch, we could measure its total Doppler factor using equipartition or SSC arguments. We could then use the measurement of δ'_f to determine the Doppler factor of the pattern, δ_p . With δ_p , μ , and $\cos \theta'$ determined, equation 5 would allow calculation of the distance to 3C 345.

2.1.4. Jet/Counter-Jet Ratio

Another potentially useful constraint is the observed jet/counter-jet brightness ratio, R , e.g. (Unwin & Wehrle 1992).

$$R = \left(\frac{1 + \beta \cos \theta}{1 - \beta \cos \theta} \right)^{n+\alpha} = (\beta_a^2 + \delta^2)^{n+\alpha} \quad (13)$$

where $n = 3$ for discrete components and $n = 2$ for continuous jet emission. The reduction of the equation to include β_a is only valid if the pattern and flow speeds are the same. If they are the same

or if we know the relationship between them, measurement of R allows us to directly compare the Doppler factor to observed proper motion and deduce the distance to the source. In the event that the pattern and flow speeds are the same, the angular size distance is given by

$$D_A = \frac{c\sqrt{R^{\frac{1}{n+\alpha}} - \delta_p^2}}{\mu(1+z)} \quad (14)$$

An attractive feature of this approach is that the final answer depends weakly on the measurement of R . For highly beamed sources, however, R is huge and even high quality VLBI measurements cannot usefully constrain it. For less beamed sources, measuring or constraining R is more promising. A major drawback to using R to connect μ and δ_p is that R is a global property of the jets rather than of an individual component. For R to be useful, the flow speed and angle to the line of sight need to be the same for the jet and counter-jet and constant over the region for which R is measured. In addition, there cannot be significant excess absorption of emission from the counter-jet, c.f. (Krichbaum et al. 1998).

2.2. Doppler Factors

The synchrotron spectral turnover provides a kind of natural (but broad) spectral line for homogeneous synchrotron sources. By carefully measuring the spectrum of a component and its angular size we can use limits on its SSC x-ray flux, e.g. (Marscher 1987) or an assumption of equipartition between the field and particle energies (Readhead 1994) to determine the Doppler factor. In the appendix these formulae are presented for arbitrary homogeneous geometry and for the specific case of a spherical geometry.

We have chosen to use a spherical component geometry for the calculations presented in this paper. Without detailed knowledge of the true geometry a spherical geometry is well-suited for calculation because it computes the angular area presented to the observer reasonably, gives a sensible line of sight through the component, and provides naturally for a range of optical depths across the component. Marscher (1987) suggests using $\theta_d \simeq 1.8\sqrt{\theta_{G_a}\theta_{G_b}}$ to convert Gaussian FWHM dimensions (measured in model-fitting) to spherical diameters, and we adopt his approximation. (See

appendix B for discussion of the effect of assumed model geometry on measured Doppler factor.)

3. Example: 3C 279

As an example of these ideas, we use a well defined component in the milli-arcsecond jet of the well known blazar 3C 279 at $z = 0.536$. We observed 3C 279 with the Very Long Baseline Array³ (VLBA) for six epochs at 15 and 22 GHz during 1996 and at four frequencies (5.0, 8.4, 15.4, and 22.2 GHz) during December of 1997. These observations were all calibrated using standard techniques, e.g. (Cotton 1993; Roberts, Wardle & Brown 1994), using the National Radio Astronomy Observatory's Astronomical Image Processing System (AIPS). Model-fitting was performed in the (u,v)-plane with the Caltech VLBI program, DIFMAP.

3.1. Proper Motion

Figure 3 shows the structure of the inner jet of 3C 279 at 22 GHz. Table 1 gives detailed component data from model-fitting the inner jet of 3C 279 for the 1997.94 epoch. K1 is a well defined, strong component which has persisted for years, e.g. (Unwin et al. 1998). The component is located approximately 3 milli-arcseconds from the core at a position angle of -115° . Over the course of our observations we observe this component to move radially from the core with a proper motion of $\mu = 0.24 \pm 0.01$ mas/year (see Figure 4). It maintains a structural position angle of $-114^\circ \pm 1^\circ$ over the course of our observations.

3.2. Synchrotron Self-Absorption Turnover

We fit the total intensity of K1 at all four frequencies in 1997.94 and have measured its spectral turnover. Figure 5 displays the fit of a synchrotron self-absorption spectrum to the data assuming a slab geometry. (Fitting the spectral shape of a homogeneous sphere gives a nearly identical result but a slightly smaller error range on the parameters.) The spectral turnover is located

³The VLBA is part of the National Radio Astronomy Observatory, which is a facility of the National Science Foundation operated under cooperative agreement by Associated Universities, Inc.

at $\nu_{peak} = 6.02$ GHz ($+0.33, -0.49$) with a flux, $S_{peak} = 4.40$ Jy ($+0.19, -0.07$), and a spectral index, $\alpha = 0.52 \pm 0.05$. The errors in the fit are approximately 1σ errors found by a Monte Carlo simulation. The simulation created and fit 1000 fictional data sets using the measured data and assuming the measurements are Gaussian distributed with 1σ deviations given by the measured error bars. The error bars on the fluxes were estimated by varying parameters in the model-fits using Jim Lovell’s *Difwrap* program, an interactive shell for the Caltech VLBI program, DIFMAP. A number of factors were used to gauge the size of the error bars including shape of the chi-square minimum, noise on the residual map, and direct comparison of model and data in the (u,v)-plane. We have no direct way of knowing if the errors estimated for the fluxes are genuinely 1σ errors; however, the spectral fit has 1 degree of freedom (4 data points and 3 parameters) so the χ^2 of the spectral fit should be near unity if the errors on the data are 1σ . The measured χ^2 of the spectral fit is 1.0.

The chief uncertainty in the measured fluxes of K1 is due the presence of its poorly defined “tail”, fit as component K2. While K1 is fit robustly by a sharp Gaussian component, K2 is more difficult to fit. This becomes more of a problem at the lower frequencies (especially 5 GHz) where K1 is not as well resolved.

To check the spectral fit for K1, we examined the spectrum of observed *fractional* linear polarization. Figure 6 displays the observed fractional polarization plotted together with a theoretical curve produced by numerical simulation. The simulation is of a homogeneous slab with the same total intensity spectrum as fit to K1. The simulation solved the full equations of polarized transfer, e.g. (Jones & O’Dell 1977), for a completely tangled magnetic field plus a small ordered component. The magnitude of the ordered component was scaled to give the observed fractional polarization at 22 GHz. To simplify the simulation, no internal Faraday rotation was allowed. It is clear that the spectrum of the fractional polarization is completely consistent with total intensity spectrum fit to K1.

3.3. Doppler Factor from Equipartition

We now use the measured angular size of K1 at 22 GHz and the fit to the spectral turnover to deduce an equipartition Doppler factor (derived in the appendix). The measured FWHM angular size at 22 GHz is $\theta_{Ga} \times \theta_{Gb} = 0.46(\pm 0.02) \times 0.20(\pm 0.01)$ mas \times mas. The error bars were estimated by varying parameters in the model-fit and by comparison to the measurements at 15 GHz and 8 GHz. We use the Doppler factor formulation for a homogeneous sphere (equation A6) with $\theta_d \simeq 1.8\sqrt{\theta_{Ga}\theta_{Gb}}$. So for K1, $\theta_d = 0.55 \pm 0.02$ mas and we obtain an equipartition Doppler factor for the *pattern* of

$$\delta_p = 19.1^{+5.9}_{-2.9} \left(\frac{\eta}{D_A} \right)^{1/7} (\delta'_f)^{-6/7} \quad (15)$$

where $\eta = U_B/U_{rp}$ is the equipartition factor ($U_B =$ magnetic field energy density; $U_{rp} =$ energy density in the radiating particles), D_A is the angular size distance in Gpc, and δ'_f is the Doppler factor of the flow as viewed by an observer co-moving with the pattern. To do this computation, we have assumed energy spectrum limits of $\gamma_1 = 10$ and $\gamma_2 = 1 \times 10^6$. For $\alpha \simeq 0.5$, the dependence on these limits is approximately $[\ln(\gamma_2/\gamma_1)]^{1/7}$.

It is interesting to compare this Doppler factor for K1 to a Doppler factor measured for the component K4. The spectral fit for K4 is given in Figure 7, we find $\nu_{peak} = 12.59$ GHz ($+0.70, -0.41$), $S_{peak} = 10.86$ Jy ($+0.40, -0.37$), and $\alpha = 0.70$ ($+0.17, -0.16$) with $\chi^2 = 0.8$. We have only an upper limit on the angular size of the component transverse to the jet direction, so we can only use the limit $\theta_d \leq 0.42 \pm 0.01$. We calculate an equipartition pattern Doppler factor,

$$\delta_p \geq 16.7^{+3.6}_{-2.1} \left(\frac{\eta}{D_A} \right)^{1/7.4} (\delta'_f)^{-6.4/7.4} \quad (16)$$

for the component K4. The dependence on the energy spectrum limits for $\alpha \simeq 0.7$ is approximately $\gamma_1^{-0.4/7.4}$. Ghisellini et al. (1993) report an SSC Doppler factor for the core of 3C 279 of $\delta_{SSC} \geq 18.0$.

3.4. Aspect Ratio

K1 is a narrow component oriented perpendicular to its position angle. At 15 and 22 GHz the

component is well resolved in both directions, at 8 GHz it is less well resolved, and at 5 GHz the component is unresolved along the direction of the jet. Assuming that the component is not oblique, the observed aspect ratio is $\zeta = 0.43 \pm 0.03$.

Component K1 shows no sign of significant obliqueness. At 22 GHz we measure its orientation to be $7^\circ \pm 11^\circ$ from perpendicular to its long term structural position angle. The high frequency linear polarization of K1 is aligned with its long term structural position angle to $-3^\circ \pm 6^\circ$. (The overall calibration of the polarization position angle for our VLBA observations in Dec. 1997 was from simultaneous VLA observations of the compact source OJ287.) Using these estimates on the obliqueness in the plane of the sky as a guide, we estimate an uncertainty in the obliqueness in the plane of observation of $\pm 5^\circ$. This uncertainty in the degree of obliqueness translates to an additional uncertainty in the measured aspect ratio, roughly $\zeta = 0.43 \pm 0.08$.

3.5. Measuring the Distance

Using our measurement of the observed proper motion, pattern Doppler factor, and aspect ratio of component K1, equation 11 gives the following limit on the angular size distance to 3C 279:

$$D_A \geq 1.8_{-0.3}^{+0.5} \eta^{1/8} \text{ Gpc} \quad (17)$$

which depends only on the equipartition factor, η . Note that we have used equation 9 and our measurement of ζ ($\geq |\cos \theta'|$) to limit the Doppler factor of the flow relative to the pattern frame to $\delta'_f \leq 1.1 \pm 0.1$. (Because we have only an upper limit on δ'_f , the upper limit on the distance (equation 12) is undetermined.)

4. Discussion

Equation 17 provides only a lower limit on the angular size distance to 3C 279. The result is a limit because we could only make use of the aspect ratio constraint. In general this technique can provide direct measurements (not just limits) for sources where some of the other constraints in Section 2.1 can be applied successfully.

The 1σ errors on this limit are +28% and -17%. These errors are dominated by the uncertainty in the spectral turnover measurement of component K1. For K1, we have only one

spectral point on the optically thick side of the turnover and this point is poorly constrained due to reduced resolution at 5 GHz. The spectral turnover for component K4 is better determined giving a Doppler factor with 1σ errors of +22% and -13%. With better frequency coverage (perhaps by using widely separated IF channels near the spectral turnover) and better angular resolution at lower frequencies (through the use of space VLBI), we believe we can eventually reduce the 1σ measurement errors on Doppler factors from equipartition and SSC techniques to $\sim 10 - 15\%$.

For our 3C 279 distance limit, the equipartition factor, η , is the most significant unknown quantity. Even though η enters to only a small factor, it is poorly constrained. Readhead (1994), when proposing the technique, argued that sources should be near equipartition ($\eta = 1$ for electron-positron jets) and suggested an error of $\sim 13\%$ in the Doppler factor for typical departures from equipartition. Singal (1986) calculated the diamagnetic effect of spiraling electrons in a magnetic field. He found that the energy density of the electrons could not exceed 6 times the energy of the magnetic field and still maintain synchrotron radiation. Bobo, Ghisellini & Trussoni (1992) repeated Singal's calculation and included a surface current term. They found that the energy density of the electrons could not exceed the energy density of the *applied* field by more than a factor of 3 although they note that the energy density of the *effective* field in the region could be much smaller than the applied field.

Another issue important to calculating precise values for equipartition Doppler factors is the cutoffs in the power law particle energy spectrum. The computed Doppler factors depend only weakly on the assumed value of the cutoffs, but different, reasonable assumptions for the cutoffs may lead to a $\sim 5 - 10\%$ uncertainty in the computed Doppler factor. Energy spectrum cutoffs can be measured or constrained, however. In Wardle et al. (1998) we used VLBI circular polarization observations to show the lower energy cutoff in 3C 279 was $\gamma_1 \leq 20$. The uncertainty in the low energy cutoff dominates when $\alpha > 0.5$.

One way around the uncertainties in assuming equipartition and energy spectrum cutoffs is to calculate Doppler factors using measured x-ray fluxes. A drawback to this approach is that the

SSC Doppler factor calculated for a given component is only a lower limit because, with the capabilities of current instruments, observed x-ray fluxes include contributions from all parts of the parsec-scale source. Such a limit is unlikely to be useful for jet components like K1 in 3C 279 which contribute a very small fraction of the total x-ray flux of the source. Assuming $\eta = 1$ and inverting equation A9 to solve for the x-ray flux of K1 yields $\simeq 0.01\mu\text{Jy}$ of 2 KeV x-rays. This flux is less than 1% of the total 2 KeV x-ray flux reported by Wehrle et al. (1998) for 3C 279 in its quiescent state in January of 1996. It is interesting to note that the capabilities of the proposed MAXIM program (<http://maxim.gsfc.nasa.gov/>) would make x-ray observation of individual jet components possible.

The final area of systematic uncertainty is the assumed geometry for the pattern. We found that we obtained essentially identical spectral fits when using the functional form for a uniform slab as for a uniform sphere, so we can safely say that the assumed geometry has little affect on the spectral fit. In appendix B we explore the remaining dependence of derived Doppler factors on assumed pattern geometry. The main result is that a spherical geometry should be a good approximation for calculational purposes and tends to produce a lower limit on the Doppler factor if the true geometry is non-spherical.

5. Application to Cosmology

The angular size distance in terms of redshift, z , Hubble constant, H_0 , matter density, Ω_M , and cosmological constant, $\Omega_\Lambda = \Lambda/(3H_0^2)$ is given by, e.g. (Carroll, Press & Turner 1992)

$$D_A = \frac{c}{H_0\sqrt{|\kappa|}(1+z)} \times \mathbb{S}(\sqrt{|\kappa|} \int_0^z [(1+z')^2(1+\Omega_M z') - z'(2+z')\Omega_\Lambda]^{-1/2} dz') \quad (18)$$

where if $\Omega_M + \Omega_\Lambda > 1$ then $\mathbb{S}(x) = \sin(x)$ and $\kappa = 1 - \Omega_M - \Omega_\Lambda$, if $\Omega_M + \Omega_\Lambda < 1$ then $\mathbb{S}(x) = \sinh(x)$ and $\kappa = 1 - \Omega_M - \Omega_\Lambda$, and if $\Omega_M + \Omega_\Lambda = 1$ then $\mathbb{S}(x) = x$ and $\kappa = 1$.

In figure 8 we plot our lower limit on the distance to 3C 279 (assuming $\eta = 1$) against two cosmological models for a flat universe ($\Omega_M + \Omega_\Lambda =$

1). The first case is consistent with recent type Ia supernovae results (Perlmutter et al. 1999; Riess et al. 1998). The second case is the standard Einstein-de Sitter universe. The Hubble constant is maintained as a free parameter which scales the ordinate of figure 8.

Our single distance limit cannot distinguish between these cosmological models; however, we can investigate whether this technique holds promise for distinguishing these cases in the future. At redshifts larger than 1.0 these cosmological models differ by as much as 30–40%. Superluminal radio sources are regularly observed at these large redshifts. For 3C 279 our lower limit has 1 σ measurement errors on the order of 20–25% and we believe it is reasonable obtain distance measures (or limits) good to $\sim 10 - 15\%$ for carefully planned observations on well selected objects. Even a handful of objects (over a range of redshift values) could provide strong constraints on cosmological models.

The systematic uncertainties (discussed in §4) in measuring the Doppler factor present the largest difficulty here. We can constrain the range of allowed values for the equipartition factor, η , by comparing distance measurements to sources at similar redshifts. To detect any systematic offset in η from unity, we must have a way of calibrating our Doppler factor measurements. Fortunately, all of the poorly constrained quantities (η , energy spectrum cutoffs, geometric dependence) can be grouped as a single multiplicative parameter in the equipartition Doppler factor. We can calibrate any systematic offset in this parameter by making distance measurements to sources at moderate redshifts (where the effects of differing cosmological models are not strong) and comparing the result to other distance measurement techniques. Such a scheme would introduce a dependence on the cosmological distance ladder, so we should actively seek other techniques for calibrating systematic effects in Doppler factor measurements.

6. Conclusions

We have demonstrated a new technique for directly measuring the distances to high redshift, superluminal radio sources. This technique involves the comparison of Doppler factor and proper motion measurements for individual jet components; we must also determine the jet angle to the line

of sight and pattern versus flow velocity. We have presented several techniques for measuring or usefully constraining these parameters. In general these techniques will be applicable only to selected sources which have jet components with the right characteristics; however, with hundreds of currently known superluminal sources and new jet components emerging frequently from many of them, it seems reasonable to assume that we will find a significant number of candidates. One interesting possibility is that some sources could have more than one component to which we can apply these techniques, giving us multiple, independent distance determinations to the same object.

To begin to usefully constrain cosmological parameters we need to obtain high quality distance measurements or limits to several sources over a range of redshift. We have performed a detailed analysis of the measurement error associated with our limit on the distance to 3C 279. We found the measurement error was $\sim 20 - 25\%$ and concluded that carefully planned, high-quality observations could reduce measurement error to $\sim 10 - 15\%$. The systematic error was more difficult to quantify, although we outlined the sources of systematic error and presented rough estimates. Applying this technique to a larger sample of sources will be important not only for probing cosmological parameters but also for investigating the sources of systematic error and how close these sources are to equipartition.

7. Acknowledgments

This work has been supported by NASA Grants NGT-51658 and NGT5-50136 and NSF Grants AST 92-24848, AST 95-29228, and AST 98-02708.

A. Doppler Factor Formulae

While the relativistic plasma in radio jets does not contain atoms and molecules whose characteristic spectra we could use to directly measure their bulk Doppler factors, they do contain a unique (but broad) spectral feature: the synchrotron self-absorption turnover. The location of the turnover due to synchrotron self-absorption depends on the magnetic field strength, particle density, and size of the emission region. For a volume of homogeneous plasma, we can use the extrapolated optically thin flux at the turnover frequency and the optical depth at the turnover frequency to solve for the magnetic field and the particle density, e.g. (Marscher 1987).

$$B = \frac{\delta_p \delta_f'}{(1+z)} C_3 \tau_m^2 \nu_m^5 S_m^{-2} \Omega^2 \quad (\text{A1})$$

and

$$K = \frac{(1+z)^{4+2\alpha}}{\delta_p^{4+2\alpha} (\delta_f')^{3+2\alpha}} C_4 \tau_m^{-(2\alpha+2)} \nu_m^{-(4\alpha+5)} S_m^{2\alpha+3} \Omega^{-(2\alpha+3)} (D_A \xi_c)^{-1} \quad (\text{A2})$$

where K is the constant in the power law particle density, $N_\gamma d\gamma = K \gamma^{-(2\alpha+1)} d\gamma$. The sign of the spectral index, α , for optically thin emission is given by $S \propto \nu^{-\alpha}$. The parameter $\Omega = \left[\frac{V'}{D_A^2 s_c'} \right]$ and $\xi_c = s_c'/D_A$, where V' is the volume in the pattern frame and s_c' is the line of sight through the center of the volume along which the optical depth at the turnover, τ_m , is defined. The *extrapolated* optically thin flux⁴ at the turnover frequency, ν_m , is given by S_m . Constants C_3 and C_4 are tabulated in table 2 for Ω in mas^2 , ν_m in GHz, S_m in Jy, D_A in Gpc, and ξ_c in mas.

Assuming we can translate the source dimensions, V' and s_c' , into observable quantities (e.g. observed angular size), these expressions provide us with two equations and three unknowns, B , K , and the Doppler factor. To solve for these quantities, it is necessary to have a third constraint. Two possibilities for a third constraint are equipartition (Readhead 1994) and Synchrotron Self-Compton (SSC) x-ray flux (Marscher 1987).

A.1. Equipartition

Equipartition assumes that the energy density of the magnetic field and the energy density of the particles are equal. We will parameterize the relationship between the energy density of the magnetic field and the energy density in the *radiating* particles:

$$U_B = \eta U_{rp} \quad (\text{A3})$$

where $U_B = B^2/8\pi$, $U_{rp} = \int mc^2 \gamma N_\gamma d\gamma$. For an electron-positron jet, $\eta = 1$ for equipartition. In an electron-proton jet, the value of η for equipartition will depend on the details of the particle acceleration within the jet. (See §4 for discussion of the value of η .)

The equipartition condition is

$$B^2/8\pi = \eta m c^2 g(\alpha, \gamma_1, \gamma_2) K, \quad (\text{A4})$$

where for $\alpha \neq 0.5$

$$g(\alpha, \gamma_1, \gamma_2) = \frac{1}{2\alpha - 1} \left(\gamma_1^{-(2\alpha-1)} - \gamma_2^{-(2\alpha-1)} \right)$$

⁴The factor by which S_m over-predicts the observed peak flux, S_o , is tabulated in table 2 for a spherical geometry.

and for $\alpha = 0.5$

$$g(\alpha, \gamma_1, \gamma_2) = \ln \left(\frac{\gamma_2}{\gamma_1} \right).$$

γ_1 and γ_2 represent the lower and upper cutoffs for the particle energy distribution.

Substituting the expressions for B and K into the equipartition condition and solving for the Doppler factor yields

$$\delta_{eq} = \delta_p (\delta'_f)^{\frac{2\alpha+5}{2\alpha+6}} = F_{eq} \tau_m^{-1} (1+z) \left[\frac{g(\alpha, \gamma_1, \gamma_2) \eta S_m^{2\alpha+7}}{D_A \xi_c \Omega^{2\alpha+7} \nu_m^{4\alpha+15}} \right]^{\frac{1}{2\alpha+6}} \quad (\text{A5})$$

where F_{eq} is tabulated in table 2 for Ω in mas^2 , ν_m in GHz, S_m in Jy, D_A in Gpc, and ξ_c in mas.

Homogeneous Sphere Geometry: The spherical geometry assumes that the components emitted from the AGN are homogeneous spheres of radiating plasma. The sphere has a radius, R , and we can define an angular diameter, $\theta_d = 2R/D_A$. Therefore $\Omega = (\pi/6)\theta_d^2$ and $\xi_c = \theta_d$. With these identifications, the equipartition Doppler factor is given by

$$\delta_{eq} = F_{eq} \tau_m^{-1} (1+z) \left(\frac{6}{\pi} \right)^{\frac{2\alpha+7}{2\alpha+6}} \left[\frac{g(\alpha, \gamma_1, \gamma_2) \eta S_m^{2\alpha+7}}{D_A (\theta_d \nu_m)^{4\alpha+15}} \right]^{\frac{1}{2\alpha+6}}. \quad (\text{A6})$$

The equipartition Doppler factor derived by Readhead (1994) has a slightly different functional form than our expression. Readhead's expression is derived by comparing observed brightness temperature, T'_b , to an (rest-frame) equipartition brightness temperature, T_{eq} : $\delta_{eq} = T'_b/T_{eq}$. For 3C 279 we can turn this expression around and calculate T_{eq} for component K1 from our measured δ_{eq} and observed brightness temperature. We find $T_{eq} = 4 \times 10^{10} K$ (for $\eta = 1$) which is close to $T_{eq} \sim 5 \times 10^{10} K$ which Readhead argues is a typical upper cutoff for powerful extra-galactic radio sources in their rest-frame.

A.2. Synchrotron Self-Compton Emission

A second possible constraint is synchrotron self-Compton x-ray flux, e.g. (Marscher 1987). The observed x-ray flux from the SSC process is given by (adapted from Rybicki & Lightman (1979))

$$S_X(\nu_c) = \Xi \frac{3\sigma_T}{8} K A(p) l'' S_m \left(\frac{\nu_m}{\nu_c} \right)^\alpha \ln \left[\frac{\nu_b}{\nu_m} \right] \quad (\text{A7})$$

where

$$A(p) = 2^{p+3} \frac{p^2 + 4p + 11}{(p+3)^2 (p+5)(p+1)} \quad p = 2\alpha + 1$$

and Ξ is a factor (~ 1) that accounts for the differences in photon number density (resulting from edge effects) within the emitting volume, l'' is the average line of sight as seen from the center of the geometry in the fluid frame, ν_b is the upper cutoff frequency of the synchrotron emission spectrum, and ν_c is the x-ray observation frequency. As defined earlier, S_m is the extrapolated, optically thin synchrotron flux at the turnover frequency, ν_m .

Substituting for K and solving for the Doppler factor gives

$$\delta_{SSC} = \delta_p (\delta'_f)^{\frac{2\alpha+3}{2\alpha+4}} = F_{SSC} S_m (1+z) \left[\frac{\Xi l'' \ln \left[\frac{\nu_b}{\nu_m} \right] \nu_m^{-(3\alpha+5)} \tau_m^{-(2\alpha+2)}}{s'_c S_X(h\nu_c)_{KeV}^\alpha \Omega^{2\alpha+3}} \right]^{\frac{1}{2\alpha+4}} \quad (\text{A8})$$

where F_{SSC} is a constant which is tabulated in table 2 for Ω in mas^2 , ν_m in GHz, S_m in Jy, and S_X in μJy .

It is important to note that, in practical application, the SSC Doppler factor is only a lower limit. With the capabilities of current instruments, observed x-ray fluxes include contributions from all parts of the parsec scale jet, thermal x-ray emission from the accretion disk, and inverse-Compton x-rays which are not the result of the SSC process. We therefore obtain only an upper limit on the SSC x-ray flux of a given component and thus a lower limit on its Doppler factor.

Homogeneous Sphere Geometry: $\Omega = (\pi/6)\theta_d^2$ and $s'_c = 2R$. Also, for a spherical geometry⁵ $l'' = R$ and $\Xi = 3/4$ (Gould 1979). Making these substitutions gives the following expression for the SSC Doppler factor:

$$\delta_{SSC} = F_{SSC} S_m (1+z) \left(\frac{6}{\pi} \right)^{\frac{2\alpha+3}{2\alpha+4}} \left[\frac{3 \ln \left[\frac{\nu_b}{\nu_m} \right] \nu_m^{-(3\alpha+5)} \tau_m^{-(2\alpha+2)}}{8 \frac{S_X (h\nu_c)_{KeV}^\alpha \theta_d^{4\alpha+6}}{}} \right]^{\frac{1}{2\alpha+4}}. \quad (\text{A9})$$

B. Choice of Model Geometry for Doppler Factor Measurements

Differences between model geometries show up in the range of optical depths across the component (which affects both τ_m and the ratio S_m/S_o) and conversion of measured Gaussian FWHM diameters, θ_G , to the angular dimensions of the assumed geometry. These conversion factors can be estimated for simple geometries by matching the second moment of their Fourier transforms which are fit in the (u,v)-plane by Gaussian models. For a uniformly bright disk, $\theta_d \simeq 1.7\theta_G$. For a homogeneous sphere, $\theta_d \simeq 1.9\theta_G$.

For the purposes of measuring the Doppler factor, the effect of having a wide range of optical depths for a homogeneous sphere nearly offsets the larger conversion factor for Gaussian measured component dimensions. If we assume that a given component is a sphere, when in reality it is a uniformly bright disk, we will calculate a Doppler factor that is about 10% too small using the equipartition formula or about 5% too small using the SSC formula. In this scenario there is an additional factor by which assuming a sphere will under-predict the Doppler factor. This factor is due to the unknown physical depth of the uniformly bright disk. For the equipartition formula, this factor comes in as $\sim (\theta_d/\xi)^{1/7}$, where ξ is the angular thickness of the disk. For the SSC formula, this factor is $\sim [(8/3)(l''/s')\Xi]^{1/5}$, where l'' is the mean line of sight as seen by a photon at the center of the disk (in the fluid frame), s' is the physical depth of the disk (pattern frame), and $\Xi \sim 1$ accounts for differences in photon density throughout the disk.

In general, the patterns we observe are likely to be some compromise between these geometries, perhaps a cylindrical disk viewed nearly edge on. Without detailed knowledge of the true geometry a spherical geometry is well-suited for calculation because it computes the angular area presented to the observer reasonably, gives a sensible line of sight through the component, and provides naturally for a range of optical depths across the component. Marscher (1987) suggests using $\theta_d \simeq 1.8\sqrt{\theta_{G_a}\theta_{G_b}}$ to convert Gaussian FWHM dimensions to spherical diameters, and we have adopted his approximation.

⁵This is strictly true only if the pattern and flow are moving with the same speed.

REFERENCES

- Biretta, J. A., Owen, F. N. & Cornwell, T. J. 1989 ApJ, 342, 128
- Biretta, J. A., Owen, F. N. & Hardee, P. E. 1983 ApJ, 274, L27
- Bobo, G., Ghisellini, G. & Trussoni, E. 1992 MNRAS, 255, 694
- Carroll, S. M., Press, W. H. & Turner E. L. 1992 ARA&A, 30, 499
- Cawthorne, T. V. & Wardle, J. F. C. 1988 ApJ, 332, 696
- Cohen, M. H., Barthel, P. D., Pearson, T. J. & Zensus, J. A. 1988 ApJ, 329, 1
- Cotton, W. D. 1993 AJ, 106, 1241
- Couderc, P. 1939 Ann. d'Astrophys., 2, 271
- Eichler, D. & Smith, M. 1983 Nature, 303, 779
- Ghisellini, G., Padovani, P., Celotti, A. & Maraschi, L. 1993 ApJ, 407, 65
- Gould, R. J. 1979 A&A, 76, 306
- Hughes, P. A., Aller, H. D. & Aller, M. F. 1985 ApJ, 298, 301
- Hughes, P. A., Aller, H. D. & Aller, M. F. 1989 ApJ, 341, 54
- Jones, T. W. & O'Dell, S. L. 1977 ApJ, 214, 522
- Kellermann, K. I. 1993 Nature, 361, 134
- Krichbaum, T. P., Alef, W., Witzel, A., Zensus, J. A., Booth, R. S., Greve, A. & Rogers, A. E. E. 1998 A&A, 329, 873
- Laing, R. A. 1980 MNRAS, 193, 439
- Lynden-Bell, D. 1977 Nature, 270, 396
- Lynden-Bell, D. & Liller, Wm 1978 MNRAS, 185, 539
- Marscher, A. P. 1987, in Superluminal Radio Sources, ed. Zensus, Z. A. & Pearson, T. J. (Cambridge: Cambridge Univ. Press), 280
- Perlmutter, S., et al. 1999 ApJ, 517, 565
- Readhead, A. C. S. 1994 ApJ, 426, 51
- Riess, A. S., et al. 1998 AJ, 116, 1009
- Roberts, D. H., Wardle, J. F. C., & Brown, L. F. 1994, ApJ, 427, 718
- Rybicki, G. B. & Lightman, A. P. 1979, Radiative Processes in Astrophysics (New York, NY: John Wiley & Sons)
- Singal A. K. 1986 A&A, 155, 242
- Tipler, F. J. (1999) ApJ**511**, 546.
- Unwin, S. C. & Wehrle, A. E. 1992 ApJ, 398, 74
- Unwin, S. C., Wehrle, A. E., Xu, W., Zook, A. C. & Marscher, A. P. (1998) in ASP Conf. Ser. 144, IAU Colloq. 164 Radio Emission from Galactic and Extragalactic Compact Sources, ed. Zensus, J. A., Taylor, G. B. and Wrobel, J. M., (San Francisco: ASP), 69
- Vermeulen, R. C. & Cohen, M. H. 1994 ApJ, 430, 467
- Wardle, J. F. C., Cawthorne, T. V., Roberts, D. H. & Brown, L. F. 1994 ApJ, 437, 122
- Wardle, J. F. C., Homan, D. C., Ojha, R. & Roberts, D. H. 1998 Nature, 395, 457
- Wehrle, A. E. et al. 1998 ApJ, 497, 178
- Yahil, A. 1979 ApJ, 233, 775

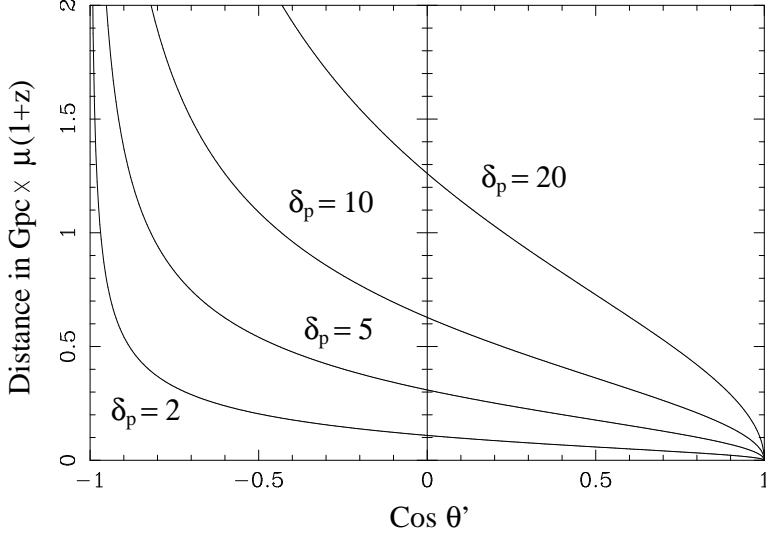


Fig. 1.— A plot of angular size distance in $\text{Gpc} \times \mu(1+z)$ versus $\cos \theta'$ where θ' is the angle of observation in the pattern frame and μ is the observed proper motion in mas/yr . The very large distances near $\cos \theta' = -1$ are a curious feature of this plot. Patterns with a negative $\cos \theta'$ are viewed from behind and travel at a larger angle than the critical angle, $\beta = \cos \theta_c$. A source which has a high Doppler factor, δ_p , and a negative $\cos \theta'$ must have a very small critical angle, θ_c . With a very small critical angle, such a source has a very large β giving it a large apparent speed, $\beta_a \propto D_A \times \mu$.

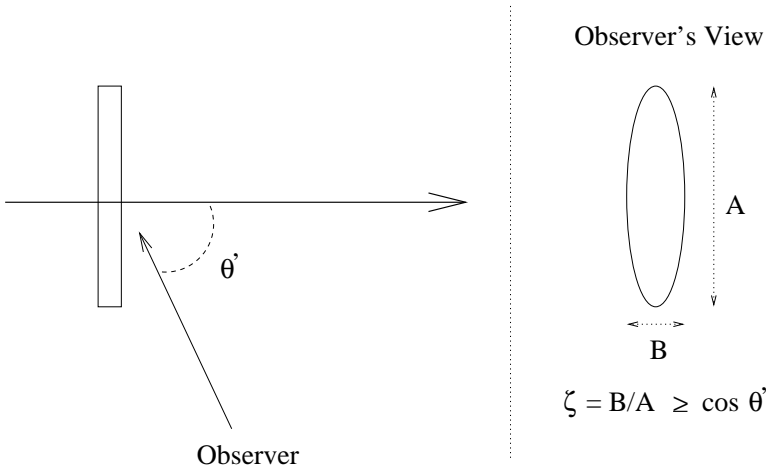


Fig. 2.— An observer sees the profile of an axially symmetric pattern from the aberrated angle, θ' . The measured aspect ratio, ζ , is always greater than or equal to $\cos \theta'$.

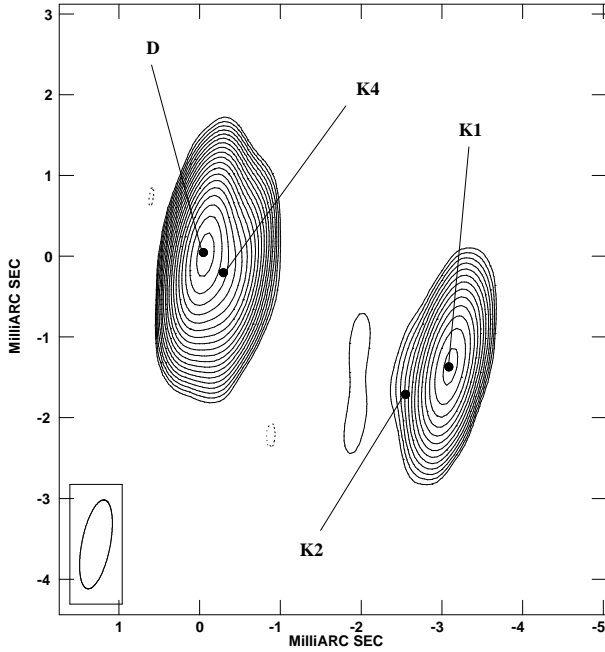


Fig. 3.— Naturally weighted image of the jet of 3C 279 at 22 GHz. Epoch 1997.94. The locations of the components K1, K2, K4, and D are marked on the image. Component data are summarized in table 1.

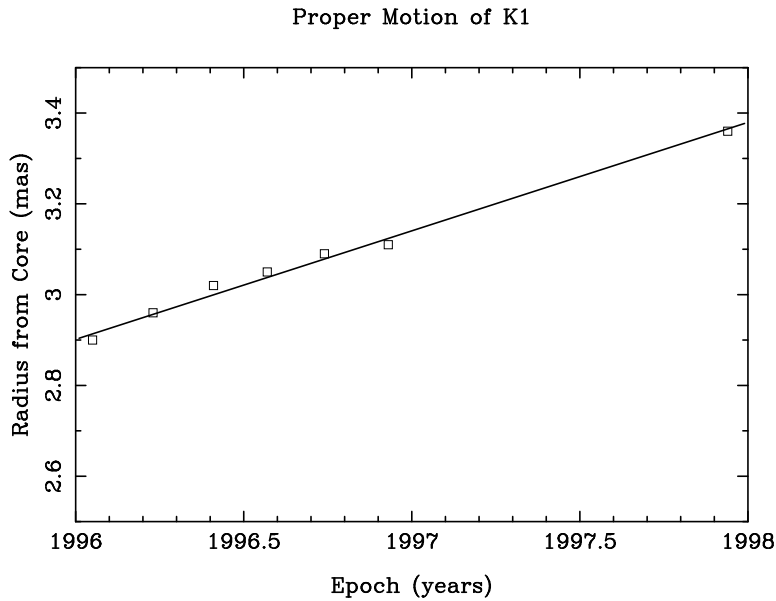


Fig. 4.— Proper motion of component K1. Component positions are taken from the 15 GHz model-fits. With the data weighted equally, the derived proper motion is $\mu = 0.24 \pm 0.01$ mas/year. Error bars on the positions are not plotted because we do not have a good a-priori method for estimating them. From the small deviation of the data from the fit, we can say that the errors in the radial position of K1 are ~ 0.02 which is about 1/20 th of the uniformly weighted beam width along that direction.

Spectral Fit for K1

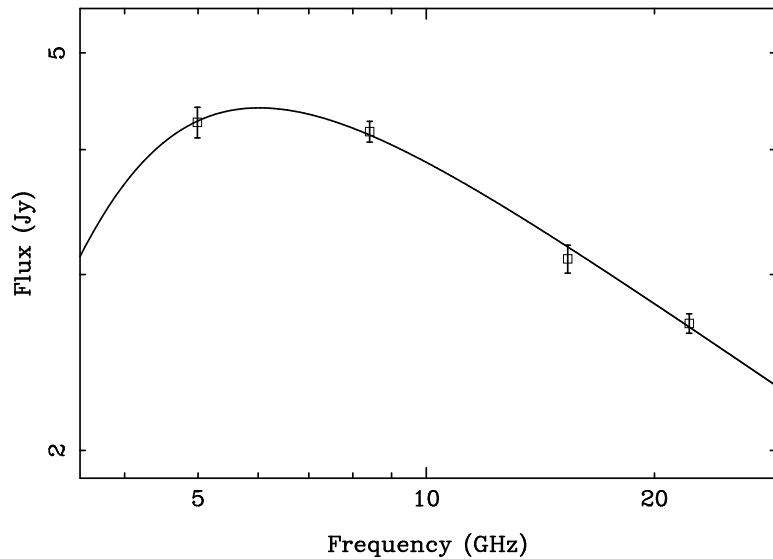


Fig. 5.— Synchrotron self-absorption spectrum of component K1. $\nu_{peak} = 6.02$ GHz (+0.33, -0.49), $S_{peak} = 4.40$ Jy (+0.19, -0.07), and $\alpha = 0.52 \pm 0.05$.

Polarization Spectrum for K1

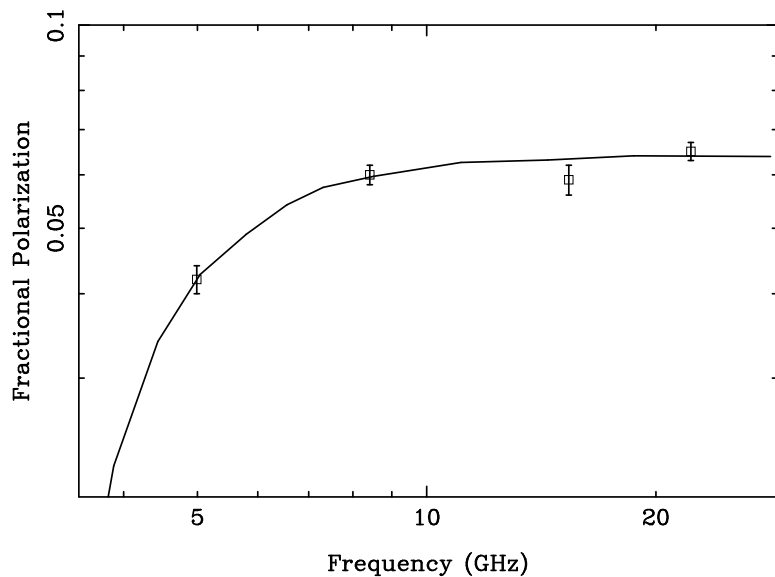


Fig. 6.— Fractional linear polarization of K1 plotted against frequency. The “theoretical curve” is from a numerical simulation of a homogeneous slab with a completely tangled magnetic field plus a small ordered component. The size of the ordered component was scaled to match the observed fractional polarization at 22 GHz. The opacity of the slab was fixed to match the fit to the total intensity spectrum.

Spectral Fit for K4

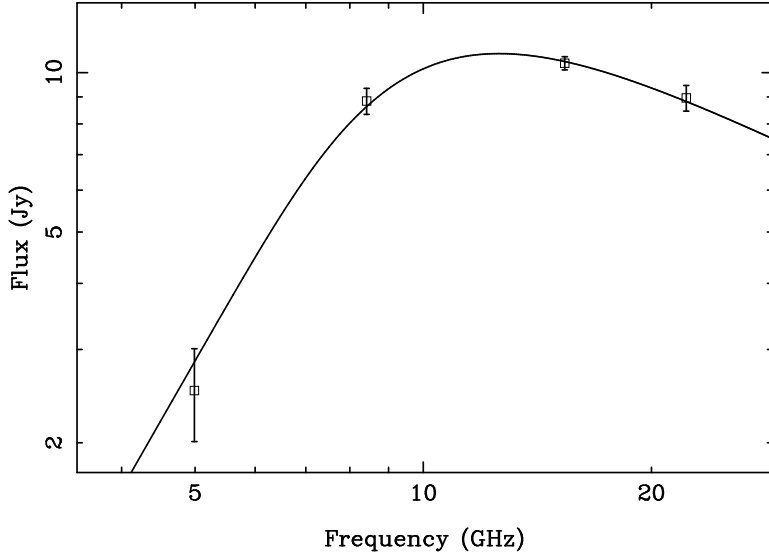


Fig. 7.— Synchrotron self-absorption spectrum of component K4. $\nu_{peak} = 12.59$ GHz (+0.70, -0.41), $S_{peak} = 10.86$ Jy (+0.40, -0.37), and $\alpha = 0.70$ (+0.17, -0.16).

Distance vs. Redshift

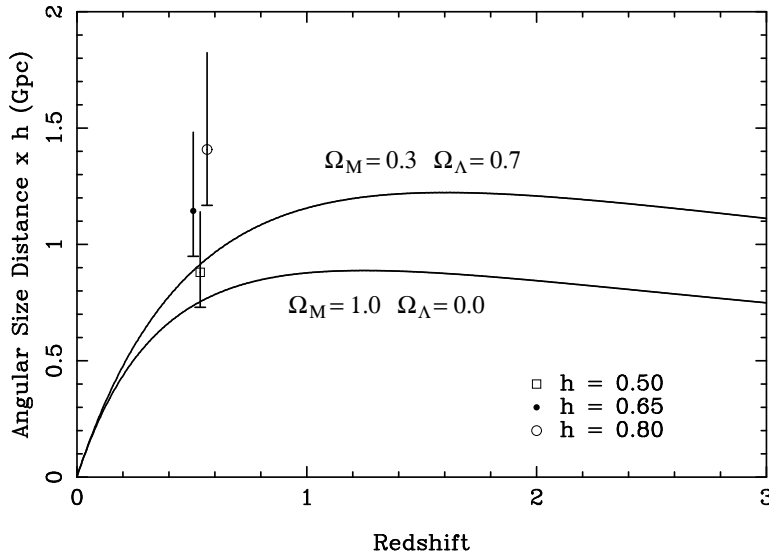


Fig. 8.— Angular size distance versus redshift for two cosmological models for a flat universe ($\Omega_M + \Omega_\Lambda = 1$). The $\Omega_M = 0.3, \Omega_\Lambda = 0.7$ case is consistent with recent SNe Ia results, and the $\Omega_M = 1.0, \Omega_\Lambda = 0.0$ case corresponds to an Einstein-de Sitter universe. The Hubble constant is taken to be $H_0 = 100h$ km/s/Mpc. Our distance limit to 3C 279 (assuming $\eta = 1$) is plotted for various values of h . The points for $h = 0.65$ and $h = 0.80$ are offset slightly in redshift to enhance readability.

Table 1: Multi-frequency Component Data for 3C 279 for epoch 1997.94.

<i>Component</i>	<i>Frequency</i> (GHz)	<i>I</i> (Jy)	<i>m_L</i> (%)	<i>χ</i> (deg)	<i>R</i> (mas)	<i>Θ</i> (deg)	<i>maj.axis</i> (mas)	<i>min.axis</i> (mas)	<i>φ</i> (deg)
D	4.99	5.20	8.9	-82
	8.42	7.31	7.4	-46
	15.37	12.08	10.6 ^a	-4 ^a
	22.23	16.27	8.2 ^a	-10 ^a	0.10	< 0.15	72
K4	4.99	2.51	3.1	-28	0.48	-121
	8.42	8.84	2.9	41	0.33	-126	0.38	< 0.50	61
	15.37	10.42	10.9 ^a	84 ^a	0.32	-132	0.37	< 0.25	71
	22.23	8.96	10.2 ^a	70 ^a	0.35	-135	0.36	< 0.15	70
K2	4.99	0.62	17.5	81	2.88	-123	1.06	< 0.30	-17
	8.42	0.29	21.2	88	2.87	-130	2.08	0.21	-30
	15.37	0.23	17.4	81	3.12	-124	1.23	0.27	7
	22.23	0.19	11.8	66	3.07	-125	1.31	< 0.07	2
K1	4.99	4.26	4.2	93	3.21	-114	0.41 ^b	< 0.30	-24
	8.42	4.17	6.0	76	3.31	-114	0.46 ^b	0.18 ^b	-27
	15.37	3.11	5.9	64	3.36	-115	0.44	0.19	-19
	22.23	2.68	6.5	63	3.37	-115	0.46	0.20	-17

NOTE.—Limits on angular size are estimated to be 1/5 of the uniformly weighted beam width along the corresponding dimension.

^aThese values were obtained by allowing the position of the core, D, to float in linear polarization and should be used with some caution.

^bThese angular dimensions appear resolved in the model-fit but are somewhat smaller than the formal limits.

Table 2: Tabulated Constants.

α	C_3	C_4	F_{eq}	F_{SSC}	τ_m	S_m/S_o
0.1	2.14×10^{-3}	1.50	1.36	1.02	0.104	1.04
0.2	1.39×10^{-3}	10.2	2.08	1.01	0.204	1.08
0.3	9.62×10^{-4}	66.3	3.02	1.00	0.300	1.12
0.4	7.01×10^{-4}	417	4.20	0.987	0.392	1.15
0.5	5.30×10^{-4}	$2.57 \times 10^{+3}$	5.67	0.972	0.480	1.19
0.6	4.12×10^{-4}	$1.56 \times 10^{+4}$	7.44	0.956	0.565	1.22
0.7	3.28×10^{-4}	$9.42 \times 10^{+4}$	9.56	0.942	0.648	1.26
0.8	2.66×10^{-4}	$5.65 \times 10^{+5}$	12.1	0.929	0.727	1.29
0.9	2.19×10^{-4}	$3.38 \times 10^{+6}$	15.0	0.918	0.804	1.33
1.0	1.82×10^{-4}	$2.02 \times 10^{+7}$	18.3	0.907	0.878	1.36
1.1	1.54×10^{-4}	$1.21 \times 10^{+8}$	22.1	0.899	0.951	1.39
1.2	1.31×10^{-4}	$7.26 \times 10^{+8}$	26.4	0.891	1.02	1.42

NOTE.—The optical depth at the turnover, τ_m , is calculated for a homogeneous sphere. The factor by which the extrapolated optically thin flux at the turnover, S_m , over-predicts the observed peak flux, S_o , is also calculated for the geometry of a homogeneous sphere.